A new index representative of seismic cracks to assess post-seismic landslide susceptibility

Shui Yamaguchi[1)]
Mio Kasai[2)]

1) Graduate School of Agriculture, Hokkaido University, Kita-9 Nishi-9, Kita-ku, Sapporo, Japan
2) Research Faculty of Agriculture, Hokkaido University, Kita-9 Nishi-9, Kita-ku, Sapporo, Japan

Conflict of interest statement: The authors declare that they have no conflict of interest.

Acknowledgements:
The authors would like to thank Shinya Katsura, Yasutaka Tanaka, and Ikkei Matsunaga for field survey assistance. We are also grateful to Kyushu Regional Development Bureau of the Ministry of Land, Infrastructure, Transport and Tourism (MLIT), and the National Research Institute for Earth Science and Disaster Prevention for providing LiDAR survey data. We thank Dr. Massimiliano Alvioli for helpful information for model evaluation. We also appreciate the insightful comments by the anonymous reviewers, which greatly improved the earlier version of this paper. This work is supported by a Grant for River and Soil Erosion Technology Research from MLIT, a Research Grant by Sabo and Landslide Technical Center and Japan Society of Erosion Control Engineering.

A new index representative of seismic cracks to assess post-seismic landslide susceptibility

Abstract

In a major earthquake, strong shaking reduces the natural soil strength. Therefore, evaluating of the susceptibility of post-seismic landslides may help prevent further disasters in an affected area. This study developed an index representing the spatial density of seismic cracks (dense crack index: DCI) to express the degree of local ground effects. An area of 6 km^2 with 196 slides identified after the 2016 Kumamoto earthquake (Mw 7.0) was analyzed using models that incorporated the weight of evidence (WoE), logistic regression (LR), and random forest (RF) methods, with the DCI as a conditioning factor. The WoE and RF models confirmed the importance of the DCI, although the improvement in performance as indicated by area under the curve values was marginal or negligible. This was largely due to combinations of other factors that enabled inclusion of locations with strong seismic waves, which compensated for the absence of the index. The contribution of the DCI could be improved if more accurate LiDAR data were used in the analysis.

Key words: Post-seismic landslides, Landslide susceptibility, Seismic cracks, Weight of

evidence, Logistic regression, Random forest, 2016 Kumamoto earthquake

Introduction

An intense earthquake can trigger numerous landslides over a wide area, causing damage to human life, property, and infrastructure. Following an earthquake, an area will remain prone to landslides, because the ground affected by strong tremors requires months to years to recover its strength. Marc et al. (2015) examined pre-, co-, and post-seismic landslides in four regions that experienced intense earthquakes with moment magnitudes of 6.6–7.6; they found that the occurrence rates of post-seismic slides were higher than pre-seismic rates until 0.7 ± 0.2 to 3.8 ± 0.9 years after the events. They concluded that this period was attributable to the intensity of the earthquakes and the recovery of hillslope strength. The number and size of post-seismic slides are usually much smaller than co-seismic slides (Marc et al., 2015), while they can still cause further disasters and disrupt safe and prompt restoration work in the affected area. Therefore, although co-seismic slides are usually a major concern from the perspective of disaster mitigation and management, the susceptibility of post-seismic slides also must be appraised immediately after an earthquake.

Susceptibility to post-seismic slides is considered related to the changes in soil structure and topographical features caused by an earthquake (Khattak et al., 2010; Massey et al., 2014; Korup et al., 2007). Changes in soil structure (e.g., soil decompaction and increased porosity) are difficult to measure directly over a wide area, while topographical features (e.g., formation and dilation of open cracks) are recognizable by field surveys and/or on aerial photographs or topographical maps derived from airborne light detection and ranging (LiDAR) surveys. Hence, in Japan, the distribution of seismic cracks is currently mapped immediately after a major earthquake using these techniques (https://www.gsi.go.jp/common/000145493.pdf). However, because the effects of such earthquakes often cover a vast area, the work itself is time-consuming and labor-intensive. In addition, image interpretation can vary according to operator skill and experience. The use of a reliable index that can digitally represent the distribution of seismic cracks could help to quickly and objectively locate slopes that are susceptible to further landslides in an emergency after a major earthquake. Cracks that are several meters in length can be expressed using a surface texture filter calculated from 1- and 2-m digital-elevation models (DEMs) based on LiDAR survey data (Kasai et al., 2009; Kasai, 2021). Assuming that soil masses with more concentrated cracks are more exposed to the earthquake and subsequently weaken, the index should also consider their spatial density, using the

surface-texture filter.

Here it should be noted that not all seismic cracks represent local slope instability. Some are formed only as a result of ground displacement, and can close over time as soil accumulates at the bottom of the crack. While it is usually recommended to monitor slopes where open cracks are clustered carefully after a major earthquake (Owen et al., 2008), the relationship between crack distribution and the occurrence of post-seismic slides has rarely been assessed, and it remains poorly understood. In addition, a field report concerning post-seismic slides after the Kumamoto earthquake (Mw 7.0) in April 2016 in Japan indicated that crack distribution should be considered together with angle and curvature of the slope in the context of slope strength (Seismic Crack Counterplan in the Tateno District: SCCTD, 2019). Here, the inclusion of an index representing clusters of seismic cracks as one of several conditioning factors (tectonics, lithology, climate, hydrology, topography, vegetation, etc.) in a statistical model would enable evaluation of the relevance of cracks and other factors to post-seismic slides (Reichenbach et al., 2018; Lee et al., 2018). For example, the WoE method allows correlations between classes of factors and landslide occurrence to be determined (Bonham-Carter, 1994; Regmi et al., 2010). The RF method can also estimate the importance of each factor with respect to

landslide occurrence.

Statistical models for landslide susceptibility have been widely applied to co-seismic slides, but only a few have been applied to post-seismic slides (Gnyawali et al., 2020). Gnyawali et al. (2020) showed that susceptibility to co-seismic landslides during the 2015 Gorkha earthquake was positively correlated with post-seismic landslides triggered by rainfall. That is, slopes severely impacted by the earthquake were more likely to collapse later. However, as in their study, the spatial resolution of the datasets commonly used in the models is often too coarse (e.g., ≥30 m) to reflect the local slope instability, which is essential for assessing the likelihood of post-seismic slides (SCCTD, 2019). For example, peak ground acceleration (PGA) and peak ground velocity are commonly employed to express seismic intensity, but spatial resolution is dependent on the distance between observation stations, which introduces uncertainty into susceptibility models (Nowicki Jessee et al., 2018; Tanyaş et al., 2019). Incorporating topographic features, such as ridges, where seismic waves are likely to be amplified (Jafarzadeh et al, 2015), together with an index that can reliably represent clusters of cracks that highlight local slope instability, is expected to contribute to improve the accuracy of susceptibility models for post-seismic landslides.

This study proposes a new index, DCI. The index represents the spatial density of seismic cracks and can be used to identify slopes vulnerable to landslides after a major earthquake. The study was conducted over a 6-km^2 area in the Aso region of Kyushu, Japan which was struck by the 2016 Kumamoto earthquake (Figure 1(a)). First, we evaluated the association of DCI values with post-seismic landslides, together with other relevant factors, using the WoE and RF methods. Then, we assessed whether inclusion of the DCI improved the performance of the model for evaluating susceptibility to landslides after an earthquake. The WoE, RF, and LR models were applied, which are widely regarded as reliable methods to assess landslide susceptibility (Brenning, 2005; Budimir et al., 2015). Finally, the current problems and possibilities for use of the DCI were considered for future applications in identifying slopes at risk of sliding immediately after a major earthquake.

Study area

The study area is located on the flank of the caldera wall of the Aso volcano and ranges in elevation from 181 m to 853 m (Figure 1(a)). According to the Aso Volcano Geological Map (1:5,000) (Ono and Watanabe, 1985), this area is entirely covered with pyroxene

andesite lava. Weathered andesitic lava covered with a thin layer of topsoil is distributed from the ridge to the nick line (Ishikawa et al.,2016a). Below the line, bedrock outcrops composed of andesite with joints occur on steep cliffs, sometimes with tuffaceous conglomerate. Colluvial slopes continue below the cliffs. These lithological features were largely similar across the study area, with local variations. In terms of vegetation, the entire area is covered with aged *Cryptomeria japonica, Quercus salicina* and *Castanopsis sieboldii*. The area is wet, with an annual rainfall average of 2,770 mm from 1989 to 2019 recorded at the Tateno observatory station operated by the Ministry of Land, Infrastructure, Transport and Tourism (MLIT) (Figure 1(b), http://www1.river.go.jp/cgi-bin/Site Info.exe?ID=109091289912020).

Landslides caused by the 2016 Kumamoto earthquake

The epicenter of the 2016 Kumamoto earthquake was 21 km southwest of the study area (Figure 1(a)), and the focus depth was 12 km (https://www.data.jma.go.jp/svd/eqev/data/2016_04_14_kumamoto/index.html). The maximum PGA of 1,791.3 cm/s^2 was observed at a location 9.7 km west of the study site (https://www.data.jma.go.jp/svd/eqev/data/kyoshin/jishin/1604160125_kumamoto/index2.html). Landslides induced by the main shock spread toward the northeast along the strike of the Futagawa Fault (https://

www.gsi.go.jp/common/000143459.pdf). In the study area, 291 co-seismic landslides were detected based on our interpretation of aerial photographs and LiDAR-derived images taken by the Kyushu Regional Development Bureau of MLIT in January 2013 and in April 2016 (immediately after the earthquake). Many seismic cracks were observed at intervals of ≤ 1 m in some places after the main shock (Ishikawa et al., 2016a). They were also visible in the LiDAR images. According to a field report by the Japan Society of Erosion Control Engineering (JSEC), most cracks were < 2 m deep, and there was no indication that surface flow was intensively supplying water to the ground through the cracks.

Ishikawa et al. (2016b) examined a series of aerial photographs (Geospatial Information Authority of Japan: GSI) taken between immediately after the main quake and July 2016 and found that most of the post-seismic slides in the area were caused by rainfall rather than the aftershocks that continued for 2 weeks along the Futagawa Fault (https://www.data.jma.go.jp/svd/eqev/data/2016_04_14_kumamoto/kumamoto_over1.pdf). First, intensive rainfall on April 21 (126 mm per day at the Tateno observatory station, Figure 2) induced several debris flows by remobilizing sediment that had collapsed during the earthquake and remained on the slopes. Continuous rainfall from June 19 to 29 (946

mm in total, with a daily maximum of 247 mm, red band in Figure 2) then caused multiple shallow translational landslides (maximum depth < 4 m). Some of these landslides subsequently triggered debris flows. However, rainfall of this magnitude is not exceptional in the region and usually does not cause landslides. For example, the last rainfall event that induced shallow landslides and debris flows was in July 2012, when the station recorded a maximum daily rainfall of 407 mm and a total of 924 mm over 2 weeks. Therefore, it was presumed that the ground strength remained weaker than usual at 2 months after the earthquake.

According to the SCCTD (2019), the topographical characteristics of the slopes where post-seismic slides were induced by the June rainfall event were steep, in the range of 40–50°. They were situated along a longitudinally convex feature (e.g., nick lines) and were horizontally concave. Clusters of seismic cracks were also recognized on the slopes. Notably, the basin area of the slope, a factor that is generally associated with the water concentration, did not appear to be related to post-seismic slide occurrences. Few landslides have been reported in the area, despite occasional heavy rains since July 2016. It was observed that sediment had begun to accumulate in the bottoms of cracks that formed on the flat tops of ridges and gentle slopes (Ishikawa et al., 2016b).

This study considered landslides that were mainly caused by reduced ground strength related to the main shock and excluded debris flows. While studies of post-seismic slides have often included debris flows induced by remobilization of loose sediment deposits generated by the earthquake (e.g., Fan et al., 2018), they were excluded because their occurrence is heavily dependent on the concentration of runoff water. However, because the type of landslides targeted could cause subsequent debris flows, the detection of slopes at risk will also aid estimates of the likely locations of debris flows.

Landslide Inventory

An inventory of co- and post-seismic landslides was compiled based on aerial photographs and LiDAR survey data acquired simultaneously in January 2013 and in April and August 2016 (Figure 1(b)). The data for August were provided by the National Research Institute for Earth Science and Disaster Prevention, NIED. Co- and post-seismic slides were mapped as polygons, after confirming that the topographic features and elevation of the area had changed apparently from the previous survey (> 1 m). Because this study investigated the effect of seismic cracks on post-seismic slides, the areas of landslide initiation were targeted for analysis; sediment transfer and deposition zones were excluded. These zones were also identified from images and elevation changes. The total number of post-seismic slides extracted was 196, with an average area of 165 m^2.

In the study area, there were slopes that appeared to be moving slowly from shallow depths. They were not included in the inventory because of difficulty confirming their

actual movement. In particular, they were shaded by trees in the aerial photographs, the spatial density of ground-survey points in the LiDAR data was insufficient to create detailed and clear images, and/or the change in elevation between surveys was sufficiently small that it could be considered a survey error.

Model analysis

Conditioning factors

Topographic, seismic, and meteorological factors were selected to construct landslide susceptibility models, as follows.

Topographic factors

Factors commonly used to assess landslide susceptibility (i.e., slope angle, plan and profile curvatures, slope aspect, and the composite topographical index [CTI]) were chosen together with the DCI. They were calculated using ArcGIS with a 1-m DEM derived from LiDAR survey data. For the DCI, two LiDAR data sets were used, one from January 2013 and one from April 2016, only the April 2016 dataset was used for the other factors.

The DCI

The DCI represents the spatial density of seismic cracks. It is derived from a surface roughness filter, based on the concept that crack formation is associated with an increase in roughness. We applied the standard deviation of slope angle for 3 × 3 cells, σ_s, proposed by Frankel and Dolan (2007), to the filter. Here, a 1-m DEM was sufficient to show cracks of several meters length, which are reportedly associated with the occurrence of post-seismic slides in the study area (Ishikawa et al., 2016a). We assumed that cracks appeared in cells where the change in standard deviation from pre- (January 2013) to post- (April 2016) earthquake ($\sigma_{s\,chg}$) was greater than or equal to a threshold value (C_m). The standard deviation of the slope angle was sensitive to the number of ground survey points; therefore, man-made structures (e.g., roads with steep edges) were excluded from the analysis because few points were expected. $\sigma_{s\,chg}$ was calculated as follows:

$$\sigma_{s\,chg} = \sigma_{s\,post} - \sigma_{s\,pre} \qquad (1)$$

where $\sigma_{s\,pre}$ and $\sigma_{s\,post}$ are the standard deviation of the slope angles in January 2013 and in April 2016, respectively. An examination of the spatial distribution of $\sigma_{s\,chg}$ and the locations where seismic ground cracks were identified in the field (Figure 3) and on topographic maps generated after the earthquake (Figure 4(a)) indicated that $\sigma_{s\,chg}$ was ≥ 2° in 75 % of the locations. This value of $\sigma_{s\,chg}$ was found in only 3 % of the locations where cracks were not identified (Figure 5). Therefore, we set C_m as 2° (Figure 4(b)).

Most of the locations with a standard deviation of ≥ 2° coincided with the seismic cracks identified in LiDAR-derived images immediately after the major earthquake. However, there were also points where these standard deviation values occurred despite the absence of apparent cracks. They were mainly false features that appeared because of errors in the filtering process from the original to the ground data. After manual correction for those points by checking against the aerial photographs, cells with $\sigma_{s\ chg} \geq 2°$ were converted into points to calculate the point density using a kernel density function for each 1-m cell. Here, a distance of 10 m was selected for the bandwidth of the function after examination of the correlation between density and the occurrence of post-seismic slides with various bands from 5 to 30 m. The density was defined as the DCI (Figure 4(c)).

Importantly, the index reflects both the size and number of cracks produced by the earthquake. Therefore, similar DCI values may be present in both a case with many small cracks and one with a few long and wide cracks. In this study, the ground was considered similarly weakened in both cases, although the strength would differ in reality. This index could be improved by collecting the width, depth, and length of a sufficient number of cracks to independently reflect their size. Unfortunately this information was difficult to obtain because of limited access to the sites.

Accuracies of the DCI and DEM

The reliability of DCI values depends on the accuracy of the DEMs used for their calculation. To check the accuracy, 140 stationary points (e.g., roads and buildings) were selected in an area of 26 km² that included the study area. This area was chosen to ensure that a sufficient number of points could be obtained. The elevation differences at the points between the DEMs for January 2013 and those for April 2016 showed that the northern side of the Futagawa Fault had moved 1 m northeast and subsided 0.4 m on average; the southern side of the fault had shifted 0.7 m southwest and uplifted 0.1 m on average. The direction of changes agreed with previous reports that it is a right lateral displacement fault with a north-south tension axis and a normal fault component (Asano and Iwata, 2016). The amount of change also agreed with previous reports that the maximum values of horizontal movement and settlement were both approximately 2 m (Moya et al., 2017). Hence, the land on both sides of the fault moved collectively in different directions, although the movement was presumed to have minimal effects on the values that represented topographic changes. Locally, 10 % of the 81 cells with an angle > 30° had an elevation difference of > 1 m (Figure 6), which was consistent with the general notion that the vertical accuracy of DEMs tends to decrease with steeper slopes

(e.g., Lacroix, 2016). In addition, there were some locations where the spatial density of the laser beam reaching the ground surface in the LiDAR survey was low and the distance between the ground points was > 1 m (i.e., larger than the DEM resolution), because of the steep slopes and dense vegetation. In such cases, the triangulated irregular network (TIN) shape used to produce the DEM remained in the images created from the LiDAR data. One-quarter (48/196) of the post-seismic landslides were located on these slopes in the 2013 image, which may limit the feasibility of properly assessing their relationship with seismically induced cracks. Particular consideration was given to these conditions when carrying out the analysis and interpreting the results.

Plan and profile curvature (PlC and PrC), slope angle (Slp) and aspect (Asp)

The plan and profile curvatures, slope angle, and aspect appeared to provide overly detailed topographic information using the 1-m DEM; they did not seem to show the effects of slope profile on landslide occurrence adequately. Therefore, we averaged these values in an area of 10 m^2 for each cell and incorporated the results into the model.

The CTI

The CTI represents potential soil wetness (Moore et al., 1991) and is derived as follows:

$$CTI = \ln\left(\frac{A}{\tan(\theta)}\right) \qquad (2)$$

where A is the contributing drainage area (m^2) and θ is the slope angle (°).

Seismic factors: Distance to the Futagawa Fault (DtF) and PGA

We used two seismic factors in this study: distance to the Futagawa Fault (DtF) and PGA. The distribution of PGA was estimated by the natural neighbor method through interpolation of a three-dimensional synthetic PGA, recorded at 98 surrounding stations established by the Japan Meteorological Agency, JMA and NIED. The closest and farthest stations were 3.6 and 117 km from the study area, respectively. Nine stations were located within 10 km of the perimeter of the study area. Due to the distance between the stations, the PGA was obtained for every 100-m cell and applied to the modeling after the values had been resampled for 1-m cells.

Meteorological factors: total rainfall (Rain)

Most of the post-seismic slides analyzed in the study area were triggered by the rainfall from June 19 to 29, 2016 (Figure 2, Ishikawa et al., 2016b). Therefore, the total rainfall for the period was selected as a meteorological factor. Its spatial distribution was

estimated by the natural neighbor method based on observations at 35 gauging stations established by JMA and MLIT, located within 30 km of the Tateno observatory station. The estimated values were assigned to each 1-m cell.

Datasets for the landslide susceptibility model

Ten datasets for modeling were created as follows. Of the 32,303 cells contained in post-seismic landslides, 70 % (22,612 cells) were randomly selected to train the model and the remaining 9,691 cells were used for testing. The same number of 1-m cells contained in the landslide polygons was also randomly selected from outside the landslide area; 70 % of each group was used for training, while the rest were used for testing. This process was repeated 10 times.

Models

The WoE method

The WoE method (Bonham-Carter, 1994; Regmi et al., 2010) is a bivariate model that allows examination of the correlation between a certain conditioning factor class and landslides. The correlation is given by the contrast, C, as follows:

$$C = W^+ - W^- \qquad (3)$$

where W^+ and W^- are the positive and negative weights of evidence for a certain class in a 1-m cell, respectively, and are given by:

$$W^+ = \ln \frac{P(F|L)}{P(F|\overline{L})} \qquad (4)$$

$$W^- = \ln \frac{P(\overline{F}|L)}{P(\overline{F}|\overline{L})} \qquad (5)$$

where L is the presence of a landslide, F is the presence of a value within a certain conditioning factor class, $\overline{L}$ is the absence of a landslide, $\overline{F}$ is the absence of a value within a certain conditioning factor class, $P(F|L)$ is the probability of a 1-m landslide cell with a value within a certain conditioning factor class, $P(F|\overline{L})$ is the probability of a cell outside of a landslide containing a value within a certain conditioning factor class, $P(\overline{F}|L)$ is the probability of a 1-m landslide cell not containing a value within a certain conditioning factor class, and $P(\overline{F}|\overline{L})$ is the probability of a cell outside of a landslide not containing a value within a certain conditioning factor class. The combination of positive W^+ and negative W^-, or high C, implies a positive relationship between landslide occurrence and that conditioning factor class, while a combination of negative W^+ and positive W^- indicates a negative relationship. If landslide occurrence is independent of the factor class, then W^+ and W^- both equal 0. The C values obtained for each conditioning factor were summed for each 1-m cell and

used as a landslide susceptibility index for the cell. The range was set to be as equal as possible; when the number of cells belonging to a class was small (< 1 % of the total), they were merged into subsequent classes to avoid biasing the results.

In this study, we did not perform a pairwise test between two conditioning factors to calculate the χ^2 statistic, which is commonly used to assess their independence (Bonham-Carter, 1994; Regmi et al., 2010). Hence, the results obtained using this method were interpreted only as a relative index of landslide susceptibility, which was similar to the approach used by Lee et al. (2018). The reason for this is as follows. In the test, the *C* value should be relatively high near the feature values associated with the occurrence of the landslide; a binary pattern (presence or absence of a landslide) was adopted using values higher or lower than the *C* value. However, this assumption was not true for all factors. For example, extremely gentle or extremely steep slopes are less prone to landslides because extremely gentle slopes may not provide sufficient driving force for the soil mass to move, while extremely steep slopes are not likely to have a well-developed soil layer that can slide.

The LR method

The LR algorithm is expressed by:

$$y = \text{logit}(P) = \text{a} + \text{b} \times DCI + \text{c} \times Slp + \text{d} \times PlC + \text{e} \times PrC + \text{f} \times CTI + \text{g} \times Asp + \text{h} \times DtF + \text{i} \times PGA + \text{j} \times Rain \quad (6)$$

where P is the probability of landslide occurrence, a, b, c, d, e, f, g, h, i and j are constants obtained by regression, and y is the dependent value for landslide occurrence (0 for absent and 1 for present). The probability of landslide occurrence is then given by:

$$P(y) = \frac{1}{1 + e^{-y}} \quad (7)$$

The variance inflation factor of the included factors ranged from 1.050 to 2.101, and multicollinearity was not detected.

The RF method

RF is an ensemble learning method proposed by Breiman et al. (2001). It has been widely applied to landslide susceptibility models in recent years (e.g., Taalab et al., 2018; Merghadi et al., 2020). Various studies have shown that it is robust to outliers and noise; it is also less prone to overfitting and exhibits both high prediction accuracy and stability

(Dou et al., 2019). Furthermore, it can manage large amounts of data and does not require any specific normalization or standardization of the variables (Dou et al., 2019). A particular advantage is its ability to estimate important conditioning factors used for determining the presence or absence of landslides. This is attractive from the perspective of disaster prevention because it indicates the factors that should be observed and/or monitored in relation to their occurrence.

In the RF method, multiple decision trees are aggregated to perform classification and prediction. In a decision tree, the binary data (presence/absence) and variables of conditioning factors are in the root node. Then, the tree grows as it splits at each node where the variable that most effectively classifies the binary data is selected by the Gini index (Breiman et al., 1984). Nodes in the tree continue to be added until there is a single response for each terminal. A decision tree alone is a weaker classifier because of its heavy dependence on the data set applied. By contrast, the RF method can compensate for this weakness by growing diverse trees on the basis of a sub-training data set created by resampling (e.g., two-thirds of the training data with replacement by bootstrap aggregation), then randomly selecting factors for each node. In this study, we implemented the RF method in MATLAB and repeated the process until 500 trees were

constructed. Then, the predicted classifications of those trees (1 for presence, 0 for absence) were averaged to estimate the probability of a post-seismic slide for each cell.

The accuracy of the RF is evaluated by averaging the “out-of-bag” error for each decision tree over the entire forest. Here, "out-of-bag" refers to data that were not selected as a sub-training dataset, (e.g., the remaining one-third of the training data). When the model is implemented by removing the conditioning factors in sequential order, the factor associated with the larger error upon removal is considered more important in the classification. This error can be used to rank the factors in order of importance for the occurrence of post-seismic slides.

Performances of the models

The performances of the models with/without use of the DCI were compared based on the area under the receiver operating characteristic curve (AUC) for true and false positive rates.

Results and Discussion

Associations of conditioning factors with occurrence of post-seismic slides

Contrasts for each factor class (WoE)

The contrasts for each factor class presented in the WoE models agreed with the topographical characteristics associated with the occurrence of post-seismic slides reported in SCCTD (2019): steep slopes in the range of 40–50°, convex longitudinally (PrC < -2) and concave horizontally (PlC < -2) with the appearance of clusters of cracks (DCI > 0.2) (Figure 7). In particular *C* for a DCI value > 0.4 was the highest among the factor classes, along with the 0–100 m of DtF, while the class with a DCI value ≤ 0.2 (sparse appearance) had a strong negative correlation with post-seismic landslide occurrence, following those of slopes < 25° (Figure 7).

The contrasts of DCI classes suggest that the formation of seismic cracks is closely related to subsequent landslides in the target area. Their presence is associated with the values of other factor classes (Figure 8). The classes generally considered to be affected by intense seismic motions, such as a strong PGA (1,050–1,150 cm/s^2) and topographical features that are likely to appear near ridgelines (i.e., PrC < -4 m^{-1}, CTI < 0, and 40–50° in the study area), had a large percentage of cells with DCI values > 0.2 in the dataset and a high positive *C*. By contrast, slopes of < 25° were extensively distributed in the lower part of the hillslopes (e.g. Figure 9); in these classes, the percentage of cells with a DCI value >

0.2 was very small (approximately 10%, Figure 8). The negative correlation of the class above 1,150 cm/s^2 with the occurrence of post-seismic slides (Figure 7) seemed to contradict the general idea that stronger shaking produces more unstable slopes, whereas gentle slopes occupied a large part of the area that experienced the PGA value (Figure 9). Although the area also contains slopes in the range of 40–50°, the occurrence of a few post-seismic landslides was likely because little or no unstable soil mass remained after the main quake. For example, after the Hokkaido Eastern Iburi earthquake in September 2018 (Mw: 6.6, PGA at max: 967.3 cm/s^2, recorded by JMA), which induced more than 6,000 landslides over an area of 440 km^2, few post-seismic slides were observed, despite subsequent severe storms and a strong aftershock in February in 2019 (MW: 5.6, PGA: 807.4 cm/s^2, recorded by JMA). This was presumably caused by the almost complete removal of unstable soil from the slopes by the 2018 earthquake, rather than a rapid recovery of ground strength.

For rainfall, *C* was positive only for the medium range of 900–950 mm, in which the percentage of cells with a DCI value > 0.2 was higher than in other classes (Figure 7). This was inconsistent with the general notion that higher rainfall is more likely to induce landslides. Therefore, landslides were presumably prone to occur in areas with more

seismic cracks, regardless of the amount of rainfall during the June event.

The relationship between the percentage of cells with a DCI value > 0.2 and the contrast of the DtF class was less clear than the relationships between other factors (Figures 7, 8), while a closer proximity to the fault tended to result in higher contrast (Figure 7). This was probably because DtF is merely a factor of distance; its value is strongly dependent on other factors involved in landslide processes. Note that the negative *C* in the class above 55°, despite the large percentage of cells with a DCI value > 0.2, was because most locations were cliffs and the spatial density of the ground survey points tended to be low in the LiDAR surveys.

Importance of each factor according to RF

The importance of each factor according to RF implied that DCI was the most influential factor for post-seismic slide occurrence, followed by slope angle and PGA (Figure 10). This is consistent with the strong likelihood or unlikelihood presented by the contrasts of these factors (Figure 7). Rain and DtF were ranked as less important than the DCI value, slope angle and PGA; although their positive and negative contrasts were similarly large. This could be attributed to their lesser involvement in seismic crack formation.

Model evaluation

Figure 11 depicts a landslide-susceptibility map. Slopes that were highly susceptible to post-seismic slides were more concentrated along the Futagawa Fault for the WoE and LR models in cases without the use of the DCI than in cases in which the index was used. There were similar differences in the RF models between cases with and without the use of the index, but the differences were much more subtle.

Table 1 shows the average AUC values of the models for all 10 datasets. For the models based on the WoE and LR methods, the values were in the range 0.8–0.9, which was regarded as excellent performance according to Hosmer and Lemeshow (2000). However, the improvement in the models by including DCI values was marginal (2–4 %). In contrast, for RF models with and without the index, the values were both > 0.9, indicating equally outstanding performance. These results appear to contradict the earlier findings, in which both the contrasts and importance values indicated that DCI is a useful index for determining the locations of slides after a major earthquake. However, as shown in Figures 7 and 8, cracks tended to form densely in specific locations where strong seismic waves were likely to have been amplified during the main shock, increasing the landslide

susceptibility at these sites. In the models, particularly models based on RF, the absence of the index could be sufficiently balanced by successfully reproducing such slopes via the combination of PGA (i.e., the approximate intensity of shaking with a coarse spatial resolution) with local topographical features that could indicate the locations. In this context, the role of the DCI in stressing local slope instability in the models was smaller than expected.

However, AUC values alone cannot reveal all of the characteristic differences among models. Figure 12 presents examples of landslides, demonstrating that the WoE and LR models with the DCI were better able to detect slopes susceptible to post-seismic slides than were those models without the index. For example, models that included the index successfully detected a small landslide that had been overlooked in our interpretation (Figure 12(A)). Landslides also tended to be delineated more clearly by RF models using the DCI, as shown in Figure 12(B). Since the DCI is used to represent fine geomorphic features, model performance could be more appropriately evaluated using a measure that can capture the difference of landslide bodies, such as the error index proposed by Carrara (1993), rather than using the AUC as an overall measure. For example, Pokharel et al. (2021) used the error index to demonstrate morphological differences of individual

landslides between inventories.

Figure 12 also shows that the models with DCI were often overly sensitive to crack emergence and overestimated landslide susceptibility. This is considered particularly problematic where the DEM did not adequately represent the actual elevation. A major limitation regarding the DCI is the uncertainty associated with LiDAR survey data. The standard deviation in slope angles is sensitive to the ground point density, which varies between surveys depending on vegetation cover, landform, survey instruments, and the filtering techniques applied to the original data. A series of LiDAR survey data is required to calculate the DCI, and older data often tend to contain higher degrees of uncertainty, due to the less-developed survey technology, compared with currently available data. In this study, one-quarter (48) of the post-seismic slides were located on slopes that maintained the shape of the TIN used to create the DEM in the 2013 image. Fourteen of these slides (29 %) contained cells with a DCI value > 0.2, while 91 % of the remaining slides (135/148 slides) contained them. Therefore, it is possible that 44 of the 48 slides had cracks formed by the main shock. As more accurate LiDAR data become available, the advantages of models that incorporate this index may become more pronounced than at present.

Evaluation of model performance was also influenced by the uncertainty of the landslide inventory. In this study, a landslide was defined as land that had subsided ‘noticeably’ since the time of the last survey; it was accompanied by the formation or expansion of bare ground. However, there were several locations at which possible shallow ground motions had occurred that could not be confirmed with available data (Figure 13(a)); they might have been successfully detected by the RF model using the DCI. Figure 13 shows a slope where the models using the index and changes in aerial images and elevation since April implied the possibility of a slide. This slope was not included in the inventory because the resolution of this part of the LiDAR data for August was too coarse to determine whether a slide actually occurred. The locations of trees in the area also appeared to move, but such subtle changes could not provide clear evidence of a slide. Thus, unless the response variable is completely "correct," which is likely impossible for a landslide inventory, the evaluation of the DCI in landslide susceptibility models must be somewhat uncertain.

The lower-than-expected contribution of the DCI to model performance could also be related to the geology of the study area, which is characterized by clastic volcanic rocks

with joints and an absence of low permeable layers comprising fine materials (e.g., tephra) in the subsurface. Although water may penetrate underground through cracks, this lithology would not allow it to be retained over time; therefore, induction of further slides because of increased pore pressure would be unlikely. This could be why few new slides were observed after the rainfall in June, despite repeated heavy rainfall events (Figure 2) and the remaining clusters of cracks. The June rainfall event might have removed most unstable soil masses that remained on steep slopes; the strength of this mass had been considerably weakened by the impact of the main quake, as suggested by dense seismic cracks. Amounts of rainfall were not positively correlated with the occurrence of post-seismic slides, implying that these unstable slopes simply needed a trigger to collapse. Hence, while Marc et al. (2015) reported that a decline in landslide occurrence after a major earthquake is associated with soil strength recovery and earthquake intensity, it would also depend on the unstable mass remaining after the initial earthquake and the frequency of rainfall capable of causing that mass to move. In such regions, the DCI can represent local slope instability factors resulting from strong seismic motions; the inclusion of this index could allow models to perform well using fewer factors than conventionally employed to indicate instability. Further research is needed regarding this topic. However, we found that one landslide had been moving continuously –this

persisted after August– on the central crater hill, where tephra is deposited inside the caldera. In this case, the water supply from the cracks created by the main quake may have raised the groundwater level due to subsurface layers of low permeability to facilitate the movement of soil masses, but further confirmatory investigation is needed. If other landslides with similar movements are present nearby, targeting them may also emphasize the importance of the DCI in models of post-seismic landslide susceptibility.

Here, it is important to consider whether the DCI is really necessary to evaluate the likelihood of landslides after a major earthquake. We recommend using the index as a predictor of susceptibility models because the contrast from the WoE analysis and the importance value from the RF model indicated a close association of DCI values with the occurrence of landslides. Its role in those models might also be more appropriately assessed with better quality LiDAR data. However, regardless of improvements to LiDAR surveying technology, we will continue to encounter similar data-error issues because landslides frequently occur on steep slopes with dense vegetation. In such cases, we found that models using machine learning techniques (e.g., RF), which can consider the interrelationships of predictors, could provide satisfactory results without counting seismic cracks. However, they may fail to account for landslides whose mobilization

depends more on increased pore water pressure than on shear stress. This is because, in this case, cracks are both the result of ground weakening and the cause of ground instability, and are actively involved in post-seismic landslide processes.

Currently, there are no appropriate post-seismic landslide susceptibility models for use in areas where a major earthquake has hit. Various models may be developed after the event, although it is difficult to apply them to other regions because of different geological, topographical, and climatic conditions (Nowicki Jessee et al., 2018). In this situation, the DCI proposed in this study will save time and labor to help identify slopes with a high risk of sliding by objectively limiting the areas that should be considered immediately after a major earthquake. For example, cells with a DCI value > 0.2 covered 0.44 km^2, which is only 7 % of the entire study area. By excluding gentle slopes < 25°, which are probably related to the angle of repose, and steep slopes > 55°, which are mainly cliffs, the area of concern was then reduced to 0.33 km^2, which included 71 % of the post-seismic slides. This proportion should improve as the error in the data decreases. In an emergency, this simple approach could be used if LiDAR survey data are available for the periods before and immediately after the earthquake.

Parker et al. (2015) reported that the regions that experienced strong ground shaking during a 1929 earthquake in the northwest South Island of New Zealand were associated with a higher susceptibility to landslides during a 1968 earthquake in the same area. Therefore, the DCI value of each slope after a major earthquake could serve as an indicator of landslide susceptibility in the next major earthquake. However, the DCI itself requires further improvement to better represent seismic cracks and locate slopes with the potential to slide. More field reports must be examined for this purpose. The values required for calculation, such as C_m and the bandwidth of the density, may vary among regions, reflecting geographical and topographical conditions. Further improvement of the index will enable prompt restoration work after major earthquakes and thereby help with disaster management in tectonically active areas.

Conclusion

A strong earthquake induces many open cracks, some of which are caused by ground displacement, while others occur on unstable slopes and show signs of subsequent landslides. In this study we proposed a new index, the DCI, which represents the spatial density of seismic cracks; it can be used to assess their associations with post-seismic slides. By introducing the DCI into the WoE and RF models together with other

topographic, seismic, and meteorological conditioning factors, we found that this index was the most important factor determining the occurrence of post-seismic slides in the 6-km^2 area struck by the 2016 Kumamoto earthquake. However, the performances of the WoE, LR, and RF models with the index were only slightly improved compared to their use without it, according to the AUC values. This could be related to errors in the LiDAR survey data that prevented the proper calculation of DCI values in some locations, including one-quarter of the post-seismic slides, and the failure to confirm the presence of all landslides, although the models suggested them. Therefore, although we expected that the presence of cracks would further accentuate the weakness of the in-situ soil mass, we believe that their contributions were underestimated in this case. In addition, the combination of features that indicated where open cracks were likely to occur, or ridgelines where seismic waves were prone to be amplified, could compensate for the absence of the DCI. This compensation was considered possible because the lithology consisted mainly of clastic volcanic rocks with joints, which did not retain water from cracks to cause further landslides. Therefore, the dense seismic cracks that formed in the area were merely evidence of ground weakening related to the earthquake; they did not actively promote further slides. The contribution of the index to assessments of post-seismic slide susceptibility is expected to be different in areas with subsurface layers of

low permeability, where water is supplied through cracks and accumulates, raising the groundwater table and facilitating soil mass movement.

In summary, this study confirmed the potential of the DCI for evaluating landslide susceptibility after a major earthquake, although further investigations are needed. The index itself also must be more thoroughly examined, considering various reference values for calculations that should vary among regions. Therefore, the future development of the index will require the collection and analysis of a wide range of field data. These studies will contribute to future disaster prevention programs in tectonically active regions.

References

Asano, K., & Iwata, T. (2016). Source rupture processes of the foreshock and mainshock in the 2016 Kumamoto earthquake sequence estimated from the kinematic waveform inversion of strong motion data. Earth, Planets and Space, 68(1), 1–11. https://doi.org/10.1186/s40623-016-0519-9

Bonham-Carter, G. F. (1994). Tools for Map Analysis: Multiple Maps. Geographic Information System for Geoscientists: Modelling with GIS. Ontario: Pergamon.

Breiman, L. Friedman, J. Olshen, R. Stone, C. (1984). "Classification and Regression Trees". Belmont, CA: Wadsworth International Group.

Breiman, L., (2001). Random Forests. Machine Learning, 45, 5–32. https://doi.org/10.1023/A:1010933404324

Brenning, A. (2005). Spatial prediction models for landslide hazards: Review, comparison and evaluation. Natural Hazards and Earth System Science, 5, 853–862. https://doi.org/10.5194/nhess-5-853-2005

Budimir, M. E. A., Atkinson, P. M., & Lewis, H. G. (2015). Seismically induced landslide hazard and exposure modelling in Southern California based on the 1994 Northridge, California earthquake event. Landslides, 12, 895–910. https://doi.org/10.1007/s10346-014-0531-8

Carrara A. (1993). Uncertainty in Evaluating Landslide Hazard and Risk. In: J. Nemec, J.M. Nigg, F. Siccardi (Ed.), Prediction and Perception of Natural Hazards. Advances in Natural and Technological Hazards Research, vol 2. Springer, Dordrecht. https://doi.org/10.1007/978-94-015-8190-5_12

Committee for Seismic Crack Counterplan in the Tateno District. (2019). Field Investigation Report. Kumamoto: Kumamoto Prefecture.

Dou, J., Yunus, A. P., Tien Bui, D., Merghadi, A., Sahana, M., Zhu, Z., Chen, C. W., Khosravi, K., Yang, Y., & Pham, B. T. (2019). Assessment of advanced random forest and decision tree algorithms for modeling rainfall-induced landslide susceptibility in the Izu-Oshima Volcanic Island, Japan. Science of the Total Environment, 662, 332–346. https://doi.org/10.1016/j.scitotenv.2019.01.221

Fan, X., Domènech, G., Scaringi, G., Huang, R., Xu, Q., Hales, T. C., Dai, L., Yang, Q., & Francis, O. (2018). Spatio-temporal evolution of mass wasting after the 2008 Mw 7.9 Wenchuan earthquake revealed by a detailed multi-temporal inventory. Landslides, 15, 2325–2341. https://doi.org/10.1007/s10346-018-1054-5

Frankel, K. L., & Dolan, J. F. (2007). Characterizing arid region alluvial fan surface roughness with airborne laser swath mapping digital topographic data. Journal of Geophysical Research: Earth Surface, 112, 1–14. https://doi.org/10.1029/2006JF000644

Gnyawali, K. R., Zhang, Y., Wang, G., Miao, L., Pradhan, A. M. S., Adhikari, B. R., & Xiao, L. (2020). Mapping the susceptibility of rainfall and earthquake triggered landslides along China–Nepal highways. Bulletin of Engineering Geology and the Environment, 79(2), 587–601. https://doi.org/10.1007/s10064-019-01583-2

Geospatial Information Authority of Japan. (2016). Distribution of fractures on the ground surface around the Futagawa Fault by aerial photo interpretation. Retrieved from https://www.gsi.go.jp/common/00014 5493.pdf

Geospatial Information Authority of Japan. (2016). Distribution of landslides in the 2016 Kumamoto earthquake (Aso, Kumomoto). Retrieved from https://www.gsi.go.jp/common/000143459.pdf

Hosmer, D. W., & Lemeshow. S. (2000). Assessing the Fit of the Model. Applied Logistic Regression. New York: John Wiley & Sons, Inc. https://doi.org/10.1002/0471722146

Ishikawa, Y., Kubota, T., Aoto, K., Ijima, Y., Ikawa, T., Ikegami, T., Ikeda, M., Ue, H., Uehara, Y., Uchimura, Y., Egawa, K., Ohishi, H., Okano, K., Kaibori, M., Katsura, S., Kato, N., Kawahara, S., Koga, S., Sakashima, T., Sagara, W., Jitousono, T., Shinohara, Y., Shimizu, O., Shimoda, Y., Suzuki, S., Suzuki, M., Seto, K., Tagata, S., Terada, H., Teramoto, Y., Dounowaki, M., Tobioka, S., Torita, E., Nakano, K., Nishikawa, T., Hanada, R., Hirakawa, Y., Fukuzuka, K., Fujisawa, Y., Fujita, M., Masaki, K., Miyata, N., Yamaguchi, K., Yamashita, S., Yamane, M., Yokoo, K. (2016a). Sediment-related disasters induced by the Kumamoto Earthquake in April 2016. Journal of the Japan Society of Erosion Control Engineering, 69(3), 55–66. https://doi.org/10.11475/sabo.69.3_55

Ishikawa, Y., Akawaza, F., Ue, H., Ohno, H., Osanai, N., Kaibori, M., Kubota, T., Koga, S., Gonda, Y., Sakashima, T., Jitousono, T., Shimizu, O., Takeshi, T., Tarukado, A., Torita, E., Nakano, K., Nishi, M., Noro, T., Hirakawa, Y., Hiramatsu, S., Fujita, M., Matsuo, S., Yamada, T. (2016b). Secondary sediment movements and secondary sediment disasters caused by rainfalls after the Kumamoto Earthquake in April 2016. Journal of the Japan Society of Erosion Control Engineering, 69(4), 25–36. https://doi.org/10.11475/sabo.69.4_01

Jafarzadeh, F., Shahrabi, M. M., & Jahromi, H. F. (2015). On the role of topographic amplification in seismic slope instabilities. Journal of Rock Mechanics and Geotechnical Engineering, 7, 163–170. https://doi.org/10.1016/j.jrmge.2015.02.009

Japan Meteorological Agency. (2016). Earthquake count table for the 2016 Kumamoto earthquake. Retrieved from https://www.data.jma.go.jp/svd/eqev/data/2016_04_14_kumamoto/kumamoto_over1.pdf

Japan Meteorological Agency. (2016). The 2016 Kumamoto Earthquake. Retrieved from https://www.data. jma.go.jp/svd/eqev/data/2016_04_14_kumamoto/index.html

Japan Meteorological Agency. (2016). Waveform data from local government seismic intensity meters. Retrieved from https://www.data.jma.go.jp/svd/eqev/data/kyoshin/jishin/1604160125_kumamoto/index2.html

Kasai, M., Ikeda, M., Asahina, T., & Fujisawa, K. (2009). LiDAR-derived DEM evaluation of deep-seated landslides in a steep and rocky region of Japan. Geomorphology, 113, 57–69. https://doi.org/10.1016/j.geomorph.2009.06.004

Kasai M. (2021) Can Repeat LiDAR Surveys Locate Future Massive Landslides?. In: Guzzetti F., Mihalić Arbanas S., Reichenbach P., Sassa K., Bobrowsky P.T., Takara K. (eds) Understanding and Reducing Landslide Disaster Risk. WLF 2020. ICL Contribution

to Landslide Disaster Risk Reduction. Springer, Cham. https://doi.org/10.1007/978-3-030-60227-7_7

Khattak, G. A., Owen, L. A., Kamp, U., & Harp, E. L. (2010). Evolution of earthquake-triggered landslides in the Kashmir Himalaya, northern Pakistan. Geomorphology, 115(1–2), 102–108. https://doi.org/10.1016/j.geomorph.2009.09.035

Korup, O., Clague, J. J., Hermanns, R. L., Hewitt, K., Strom, A. L., & Weidinger, J. T. (2007). Giant landslides, topography, and erosion. Earth and Planetary Science Letters, 261(3–4), 578–589. https://doi.org/10.1016/j.epsl.2007.07.025

Lacroix, P. (2016). Landslides triggered by the Gorkha earthquake in the Langtang valley, volumes and initiation processes the 2015 Gorkha, Nepal, Earthquake and Himalayan Studies: First Results 4. Seismology. Earth, Planets and Space, 68(1), 1–10. https://doi.org/10.1186/s40623-016-0423-3

Lee, J. H., Sameen, M. I., Pradhan, B., & Park, H. J. (2018). Modeling landslide susceptibility in data-scarce environments using optimized data mining and statistical methods. Geomorphology, 303, 284–298. https://doi.org/10.1016/j.geomorph.2017.12.007

Marc, O., Hovius, N., Meunier, P., Uchida, T., & Hayashi, S. (2015). Transient changes of landslide rates after earthquakes. Geology, 43(10), 883–886. https://doi.org/10.1130/G36961.1

Massey, C. I., Della Pasqua, F., Taig, T., Lukovic, B., Ries, W., Heron, D., & Archibald, G. (2014). Canterbury Earthquakes 2010/11 Port Hills Slope Stability: Risk assessment

for Redcliffs. Lower Hutt: GNS Science

Merghadi, A., Yunus, A. P., Dou, J., Whiteley, J., ThaiPham, B., Bui, D. T., Avtar, R., & Abderrahmane, B. (2020). Machine learning methods for landslide susceptibility studies: A comparative overview of algorithm performance. Earth-Science Reviews, 207(May), 103225. https://doi.org/10.1016/j.earscirev.2020.103225

Ministry of Land, Infrastructure, Transport and Tourism. (2020). Water Information System. Retrieved from http://www1.river.go.jp/cgi-bin/SiteInfo.exe?ID=10909128991 2020

Moore, I. D., Grayson, R. B., & Ladson, A. R. (1991). Digital terrain modelling: A review of hydrological, geomorphological, and biological applications. Hydrological Processes, 5, 3–30. https://doi.org/10.1002/hyp.3360050103

Moya, L., Yamazaki, F., Liu, W., & Chiba, T. (2017). Calculation of coseismic displacement from lidar data in the 2016 Kumamoto, Japan, earthquake. Natural Hazards and Earth System Sciences, 17(1), 143–156. https://doi.org/10.5194/nhess-17-143-2017

Nowicki Jessee, M. A., Hamburger, M. W., Allstadt, K., Wald, D. J., Robeson, S. M., Tanyaş, H., Hearne, M., & Thompson, E. M. (2018). A Global Empirical Model for Near-Real-Time Assessment of Seismically Induced Landslides. Journal of Geophysical Research: Earth Surface, 123, 1835–1859. https://doi.org/10.1029/2017JF004494

Ono K., Watanabe K. (1985). Geological Map of Aso Volcano. Geological Map of Volcanoes, 4, Geol. Surv, Japan

Owen, L. A., Kamp, U., Khattak, G. A., Harp, E. L., Keefer, D. K., & Bauer, M. A. (2008). Landslides triggered by the 8 October 2005 Kashmir earthquake. Geomorphology, 94(1–

2), 1–9. https://doi.org/10.1016/j.geomorph.2007.04.007

Parker, R. N., Hancox, G. T., Petley, D. N., Massey, C. I., Densmore, A. L., & Rosser, N. J. (2015). Spatial distributions of earthquake-induced landslides and hillslope preconditioning in the northwest South Island, New Zealand. Earth Surface Dynamics, 3, 501–525. https://doi.org/10.5194/esurf-3-501-2015

Pokharel, B., Alvioli, M., & Lim, S. (2021). Assessment of earthquake-induced landslide inventories and susceptibility maps using slope unit-based logistic regression and geospatial statistics. Scientific Reports, 11(1), 1–15. https://doi.org/10.1038/s41598-021-00780-y

Regmi, N. R., Giardino, J. R., & Vitek, J. D. (2010). Modeling susceptibility to landslides using the weight of evidence approach: Western Colorado, USA. Geomorphology, 115, 172–187. https://doi.org/10.1016/j.geomorph.2009.10.002

Reichenbach, P., Rossi, M., Malamud, B. D., Mihir, M., & Guzzetti, F. (2018). A review of statistically-based landslide susceptibility models. Earth-Science Reviews, 180, 60–91. https://doi.org/10.1016/j.earscirev.2018.03.001

Taalab, K., Cheng, T., & Zhang, Y. (2018). Mapping landslide susceptibility and types using Random Forest. Big Earth Data, 2(2), 159–178. https://doi.org/10.1080/20964471.2018.1472392

Tanyaş, H., Rossi, M., Alvioli, M., Westen, C. J. Van, & Marchesini, I. (2019). A global slope unit-based method for the near real-time prediction of earthquake-induced landslides. Geomorphology, 327, 126–146. https://doi.org/10.1016/j.geomorph.2018.10.022

Table 1: Average AUC values of the datasets calculated for training and testing data with and without the DCI for each model.

Model	**Training data**		**Testing data**	
	with DCI	without DCI	with DCI	without DCI
WoE	0.891	0.868	0.890	0.867
LR	0.896	0.859	0.895	0.857
RF	0.999	0.999	0.997	0.997

§ AUC: area under the curve; DCI dense crack index; WoE: weight of evidence; LR: logistic regression; RF: random forest.

Figure legends

Figure 1: Study area. (a) Map of the Aso region of Kyushu, Japan. The epicenter of the 2016 Kumamoto earthquake is indicated by a red cross. (b) Landslides induced in and after the 2016 Kumamoto earthquake. The study area is outlined in black. The red dot indicates the Tateno observatory station.

Figure 2: Daily rainfall at Tateno observatory station (Figure 1(b)) from April 1 to September 30, 2016. The red band indicates the period from 19-29 June.

Figure 3: A seismic crack at the location indicated by a black circle in Figure 4. The crack was 60 cm in width and 85 cm in depth. The photograph was taken in December 2019.

Figure 4: An example of earthquake-induced changes in the ground surface. The extent of the area is indicated by the white square in Figure 1(b). The location of the lower images is shown in the upper images by the white square. (a) Slope maps before and after the earthquake, derived from LiDAR survey data. (b) Cells with $\sigma_{s\,chg} \geq 2$. (c) Distribution of DCI values. The location of the crack shown in Figure 3 is indicated by a black circle. In (b) and (c), the background is the gray-scale slope image in April 2016 and black lines

indicate cracks in April 2016.

DCI: dense crack index.

Figure 5: Box plots of $\sigma_{s\ chg}$ for locations where cracks were and were not identified. The interquartile range is represented by the box. Upper whiskers: 1.5 times the interquartile range above the third quartile. Lower whiskers: 1.5 times the interquartile range below the first quartile. Outliers are plotted as dots. Crosses are the averages of $\sigma_{s\ chg}$ and the horizontal line represents the median value.

Figure 6: Relationship between slope angle before the Kumamoto earthquake and the absolute difference between the DEMs for January 2013 and April 2016.

Figure 7: Contrasts of the conditioning factors and proportion of cells with DCI values > 0.2 for each factor class.

DCI: dense crack index; Slp: slope angle; PlC: plane curvature; PrC: profile curvature; CTI: compound topographic index; Asp: slope aspect; DtF: distance to Futagawa Fault; PGA: peak ground acceleration; Rain: total rainfall.

Figure 8: Relationship between the proportion of cells with DCI values > 2 in a class and the average contrast value of the dataset.

DCI: dense crack index; Slp: slope angle; PlC: plane curvature; PrC: profile curvature; CTI: compound topographic index; Asp: slope aspect; DtF: distance to Futagawa Fault; PGA: peak ground acceleration; Rain: total rainfall.

Figure 9: Enlarged view of a slope map for the area where PGA ≥ 1,150 cm/s^2. The area is in the blue square in Figure 1(b).

Slp: slope angle.

Figure 10: Importance values of the conditioning factors that influence the occurrence of post-seismic landslides.

DCI: dense crack index; Slp: slope angle; PlC: plane curvature; PrC: profile curvature; CTI: compound topographic index; Asp: slope aspect; DtF: distance to Futagawa Fault; PGA: peak ground acceleration; Rain: total rainfall.

Figure 11: Landslide susceptibility maps using dataset 1 obtained with and without DCI for the WoE, LR and RF models.

DCI: dense crack index; WoE: weight of evidence; LR: logistic regression; RF: random forest.

Figure 12: Examples of post-seismic slides (outlined in green). The locations of (A) and (B) are indicated by the red and black cross respectively in Figure 11. The landslide shown in (A) was overlooked in our interpretation. The locations of (A) and (B) are indicated by the red and black crosses, respectively, in Figure 11. The landslide shown in (A) was overlooked in our interpretation. (a) Gray-scale slope maps and photographs for April and August 2016. (b) Cells in the top 0.06 % for susceptibility level (colored red) identified by the WoE, LR, and RF models. The background is the gray-scale slope map for August 2016. No landslide was found in the red cells located outside the polygons.

DCI: dense crack index; Slp: slope angle; WoE: weight of evidence; LR: logistic regression; RF: random forest.

Figure 13: An example of a possible slide suggested by the RF model with the DCI (outlined in pale blue). The location is indicated by the white cross in Figure 11 (RF model with DCI). (a) Slope maps and aerial photographs for April and August 2016. (b) Red cells are the top 0.06 % of the susceptibility level by the RF model. (c) The difference in

DEMs from April to August 2016.

DCI: dense crack index; Slp: slope angle; RF: random forest.

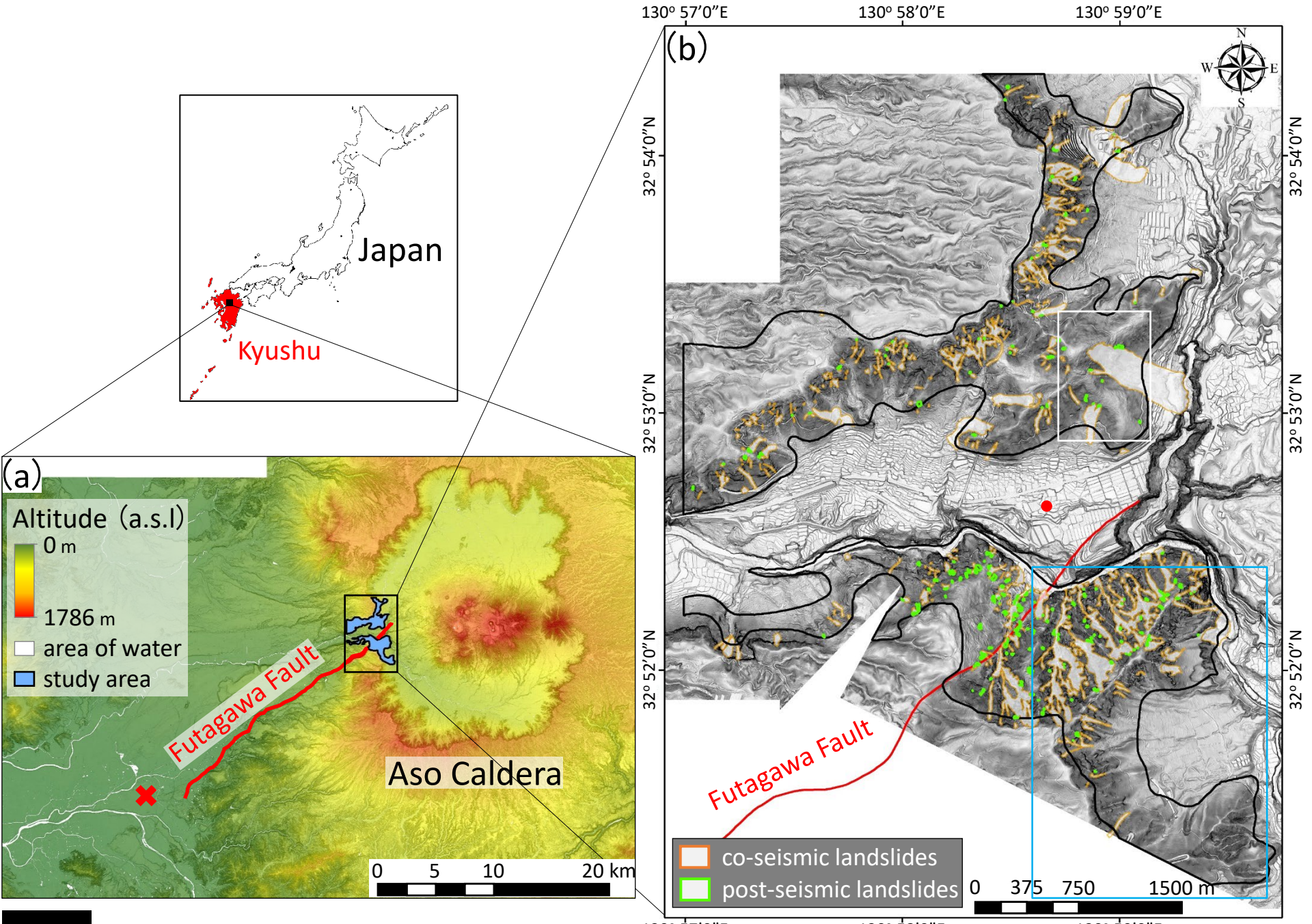
Japan
Kyushu
(a)
Altitude (a.s.l)
0 m
1786 m
area of water
study area
Futagawa Fault
Aso Caldera
0 5 10 20 km
(b)
130° 57′0″E
130° 58′0″E
130° 59′0″E
32° 54′0″N
32° 53′0″N
32° 52′0″N
N
W
E
S
Futagawa Fault
co-seismic landslides
post-seismic landslides
0 375 750 1500 m

Fig 1

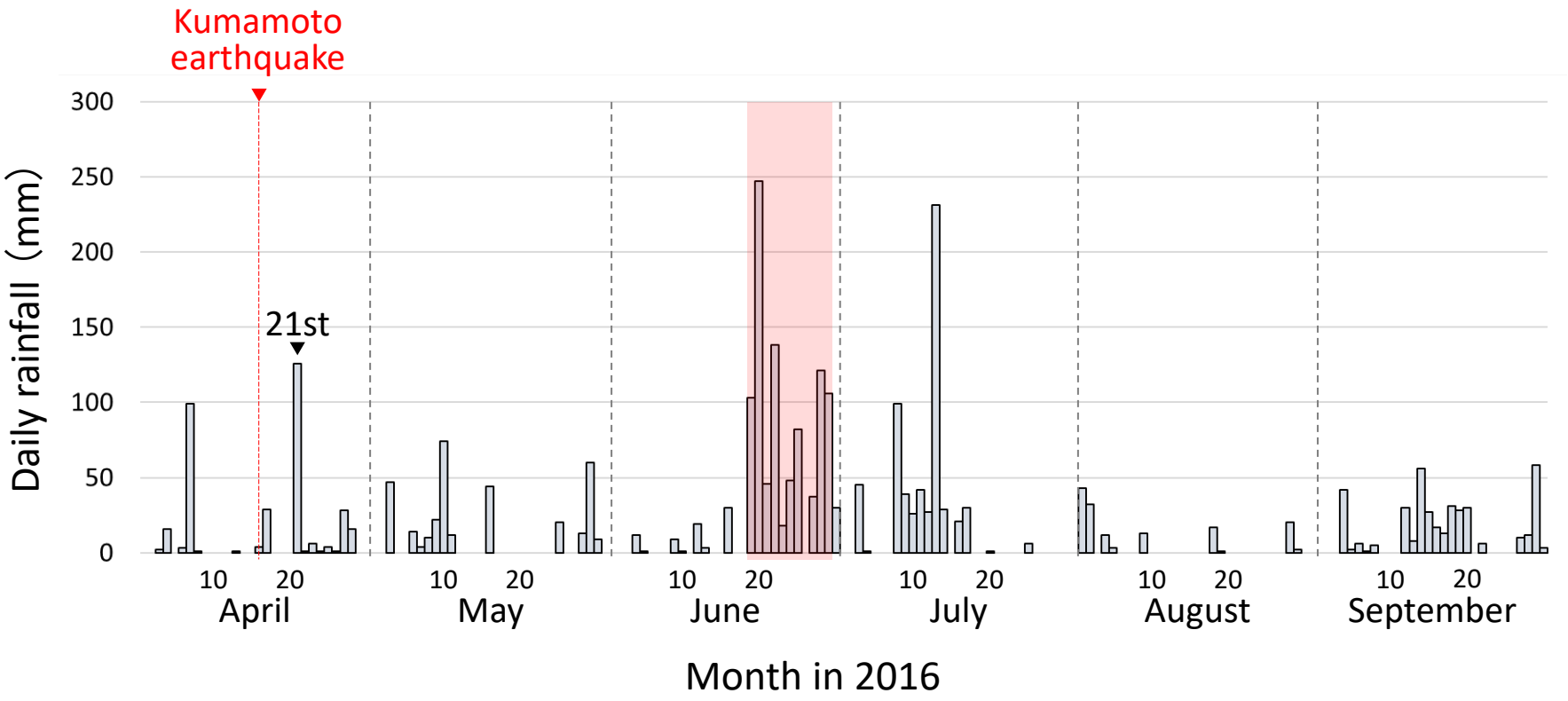
Kumamoto
earthquake
21st
Daily rainfall (mm)
300
250
200
150
100
50
0
10
20
April
May
June
July
August
September
Month in 2016

Fig 2

Fig 3

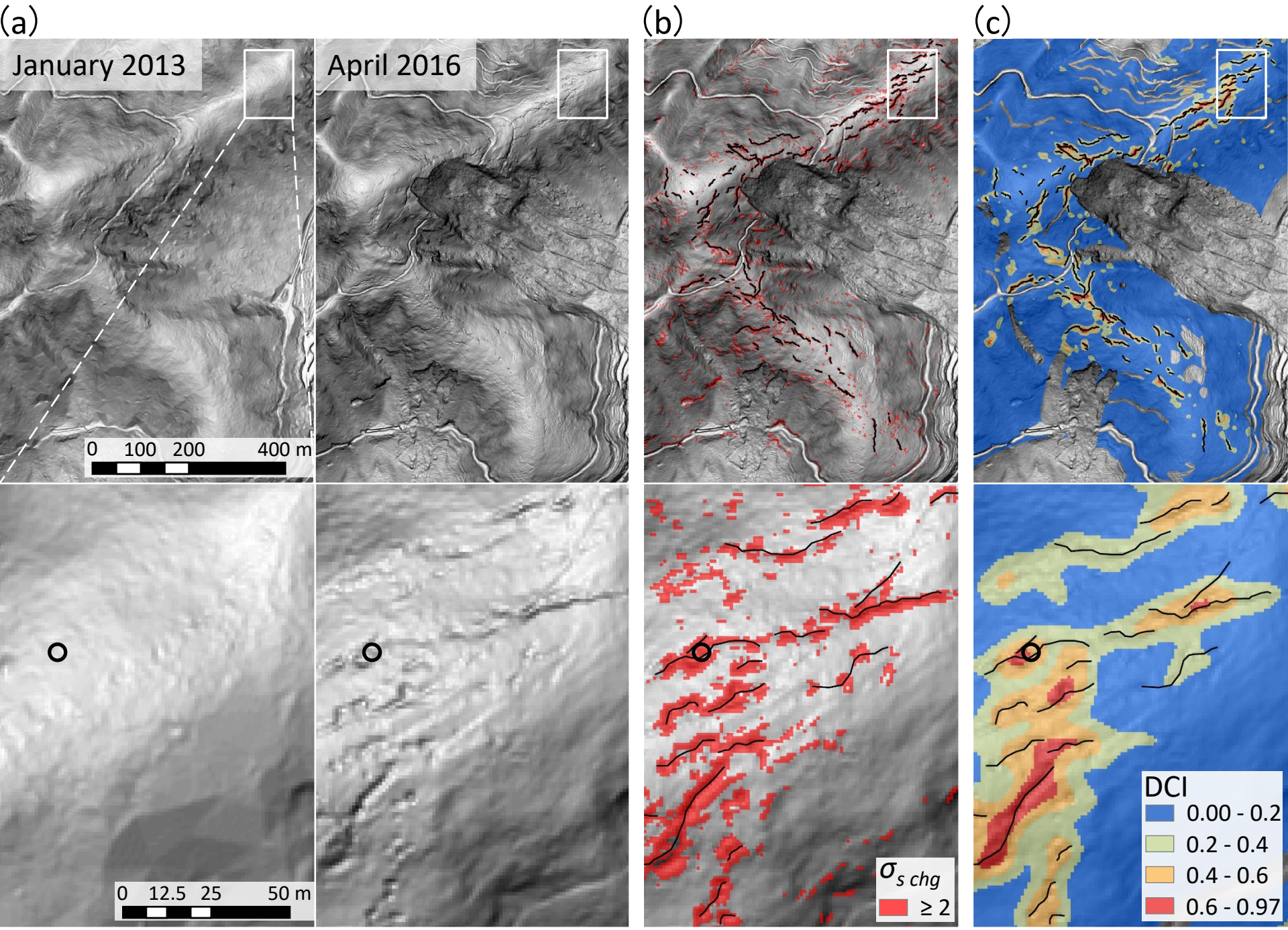
(a)
January 2013
April 2016
0 100 200 400 m
0 12.5 25 50 m
(b)
$\sigma_{s\ chg}$
≥ 2
(c)
DCI
0.00 - 0.2
0.2 - 0.4
0.4 - 0.6
0.6 - 0.97

Fig 4

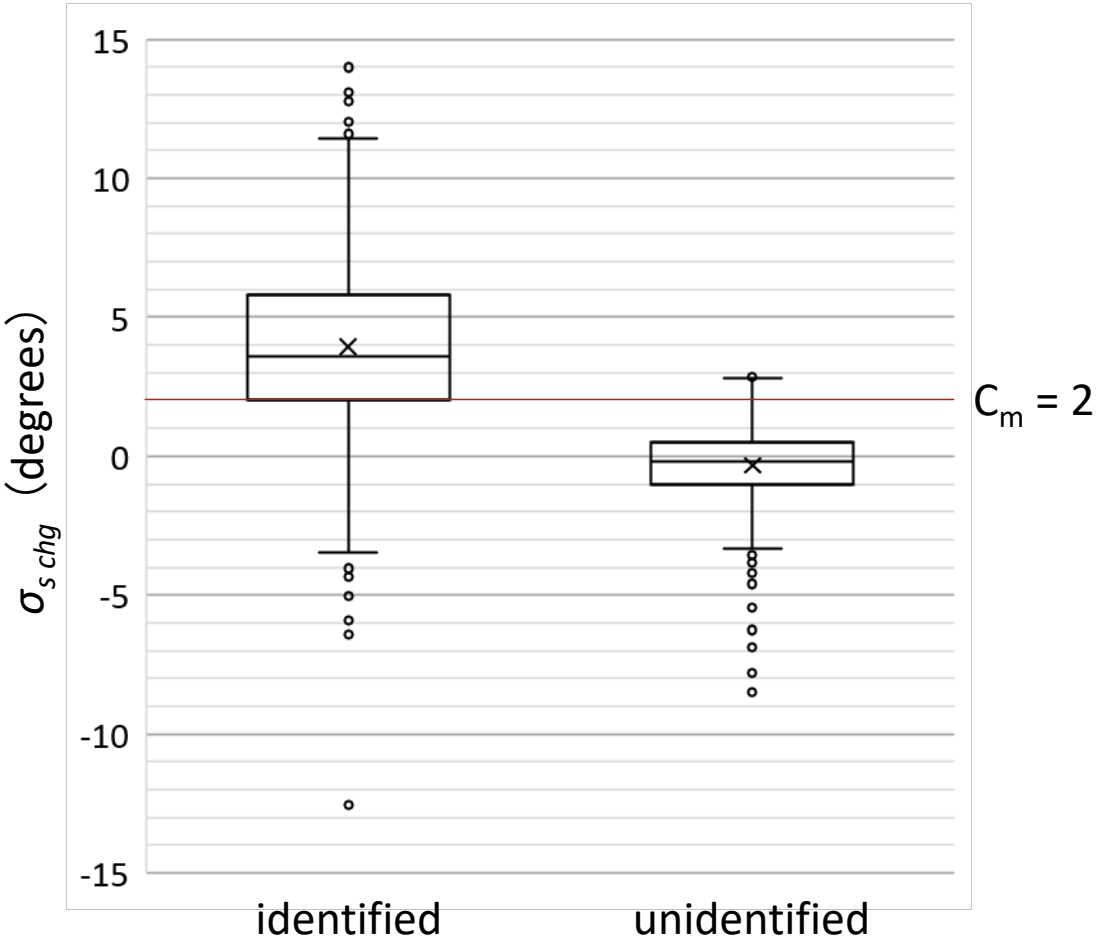
15
10
5
0
-5
-10
-15
$\sigma_{s\,chg}$ (degrees)
C_m = 2
identified
unidentified

Fig 5

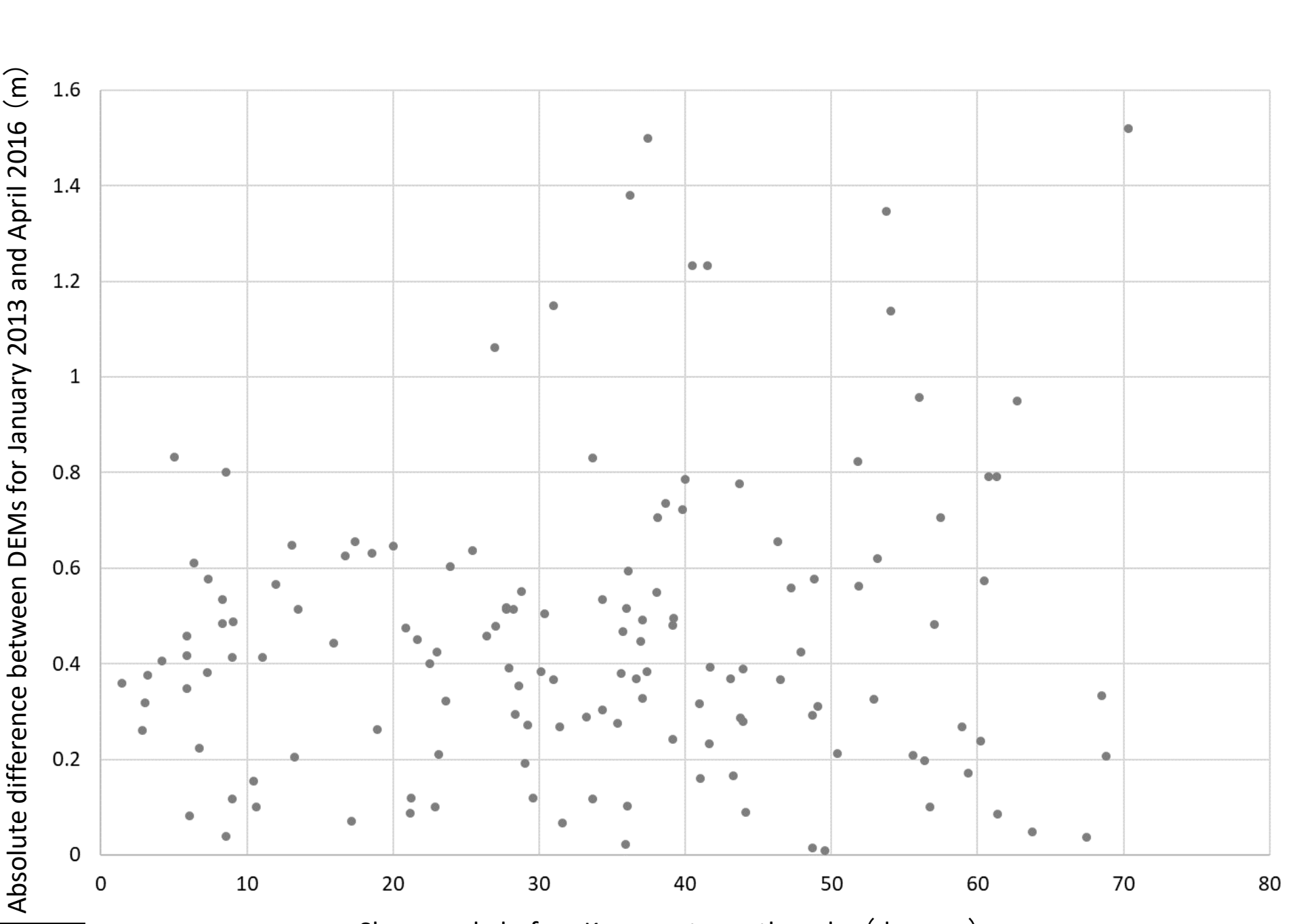
Absolute difference between DEMs for January 2013 and April 2016（m）
1.6
1.4
1.2
1
0.8
0.6
0.4
0.2
0
0
10
20
30
40
50
60
70
80
Slope angle before Kumamoto earthquake（degrees）

Fig 6

Fig 7

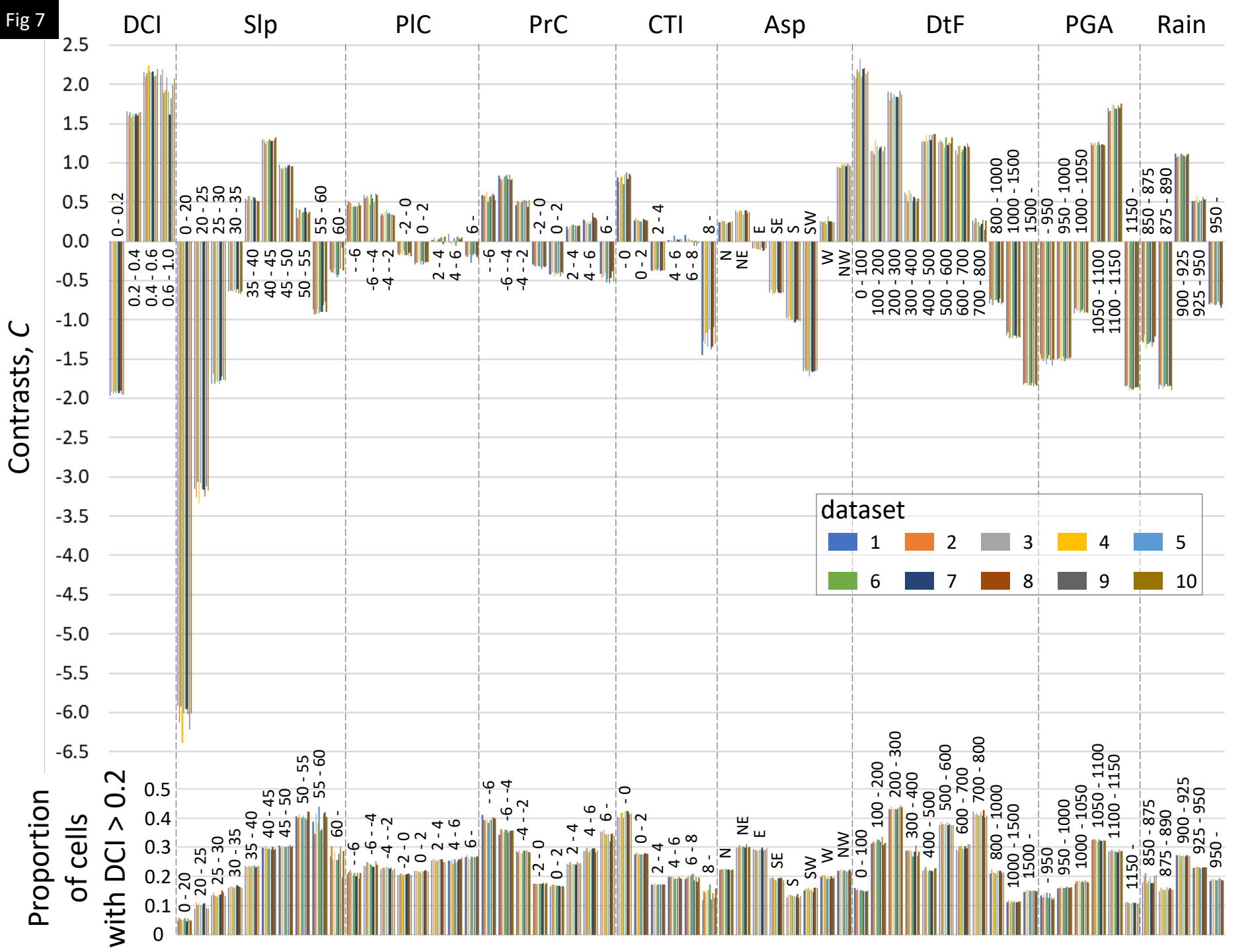
DCI
Slp
PlC
PrC
CTI
Asp
DtF
PGA
Rain
Contrasts, C
2.5
2.0
1.5
1.0
0.5
0.0
-0.5
-1.0
-1.5
-2.0
-2.5
-3.0
-3.5
-4.0
-4.5
-5.0
-5.5
-6.0
-6.5
dataset
1
2
3
4
5
6
7
8
9
10
Proportion of cells with DCI > 0.2
0.5
0.4
0.3
0.2
0.1
0

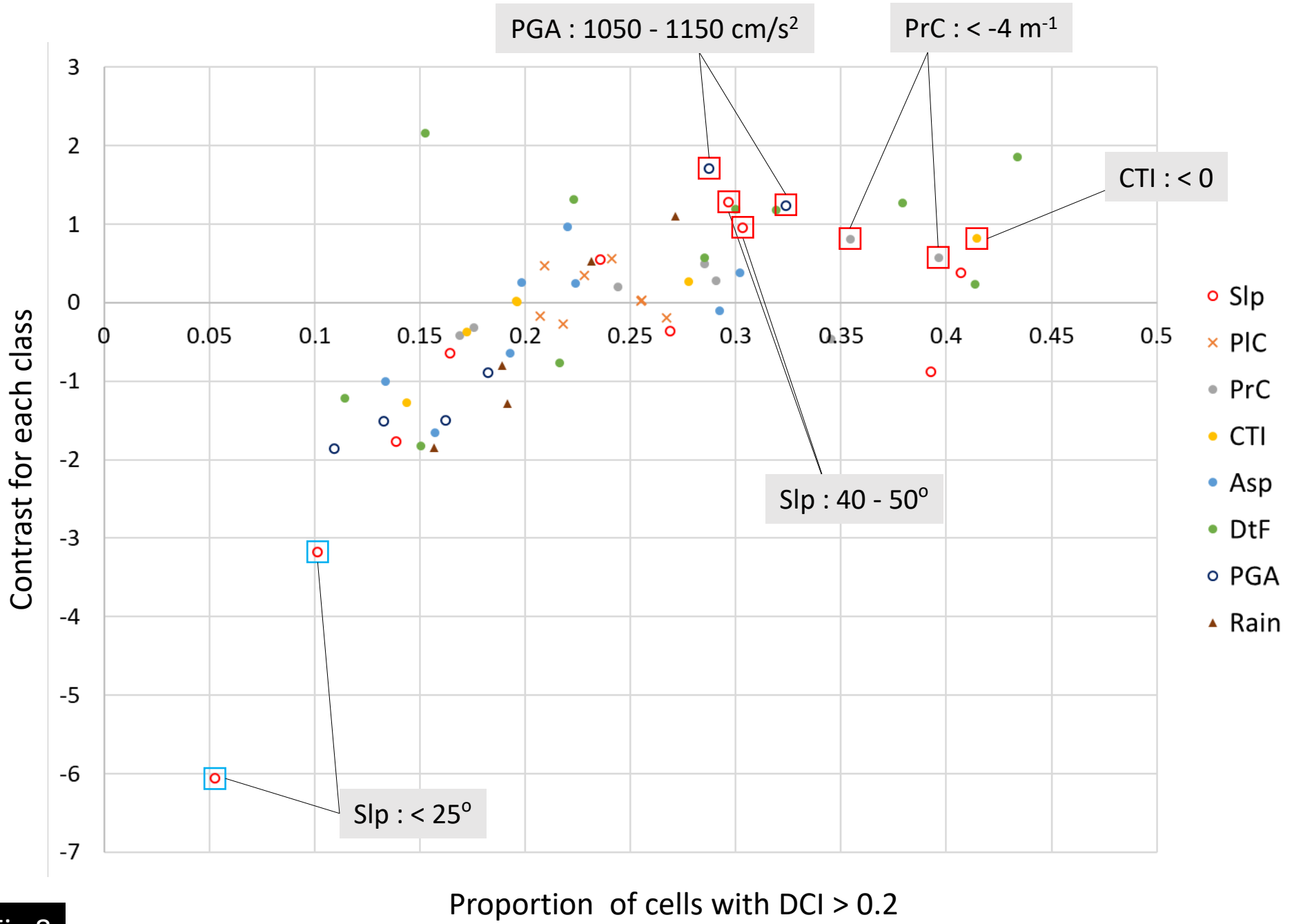
PGA : 1050 - 1150 cm/s²
PrC : < -4 m⁻¹
CTI : < 0
Slp : 40 - 50°
Slp : < 25°
Contrast for each class
Proportion of cells with DCI > 0.2
3
2
1
0
-1
-2
-3
-4
-5
-6
-7
0
0.05
0.1
0.15
0.2
0.25
0.3
0.35
0.4
0.45
0.5
Slp
PIC
PrC
CTI
Asp
DtF
PGA
Rain

Fig 8

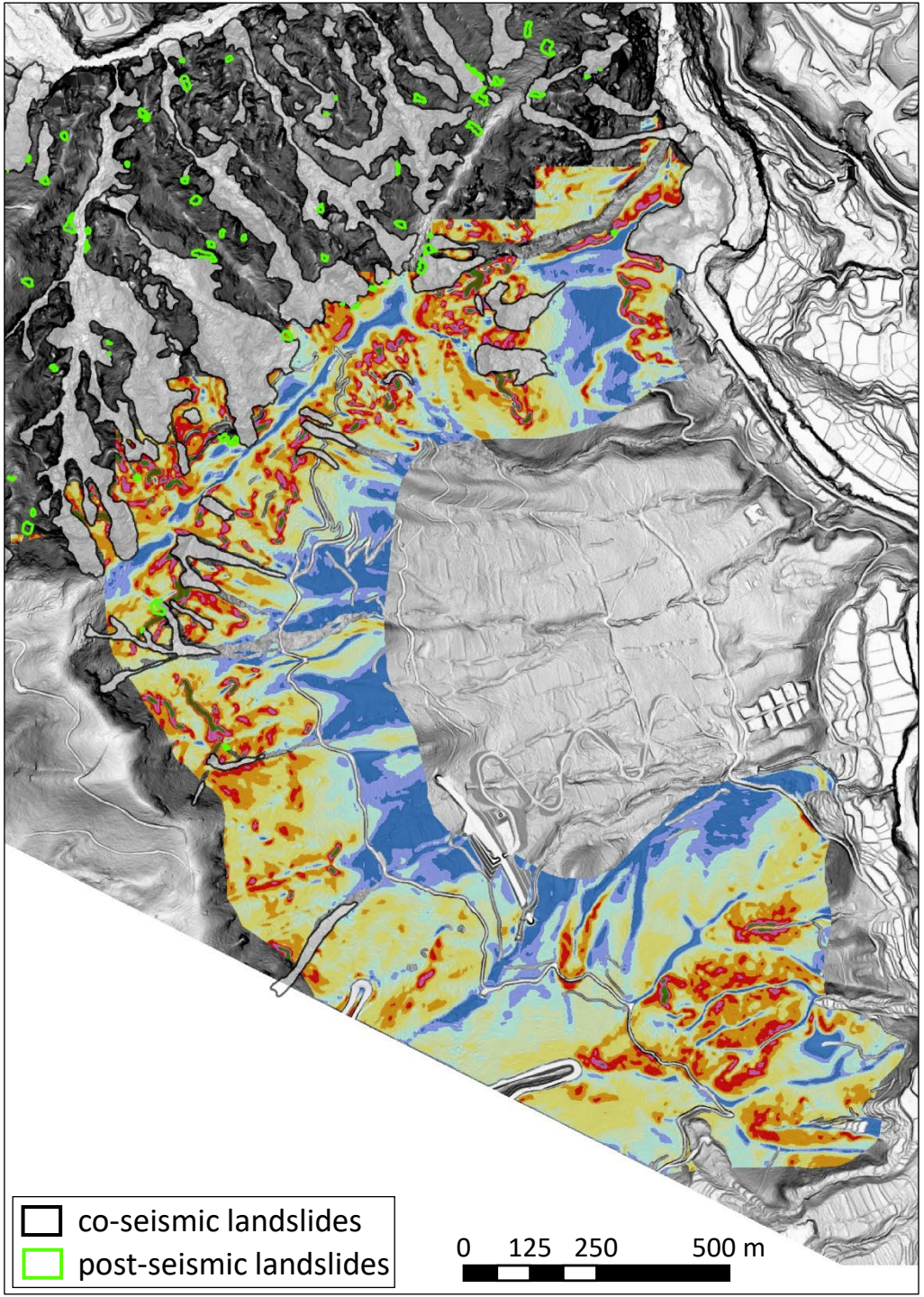
co-seismic landslides
post-seismic landslides
0 125 250 500 m
Slp（degrees）
0 - 20
20 - 25
25 - 30
30 - 35
35 - 40
40 - 45
45 - 50
50 - 55
55 - 60
60 - 80

Fig 9

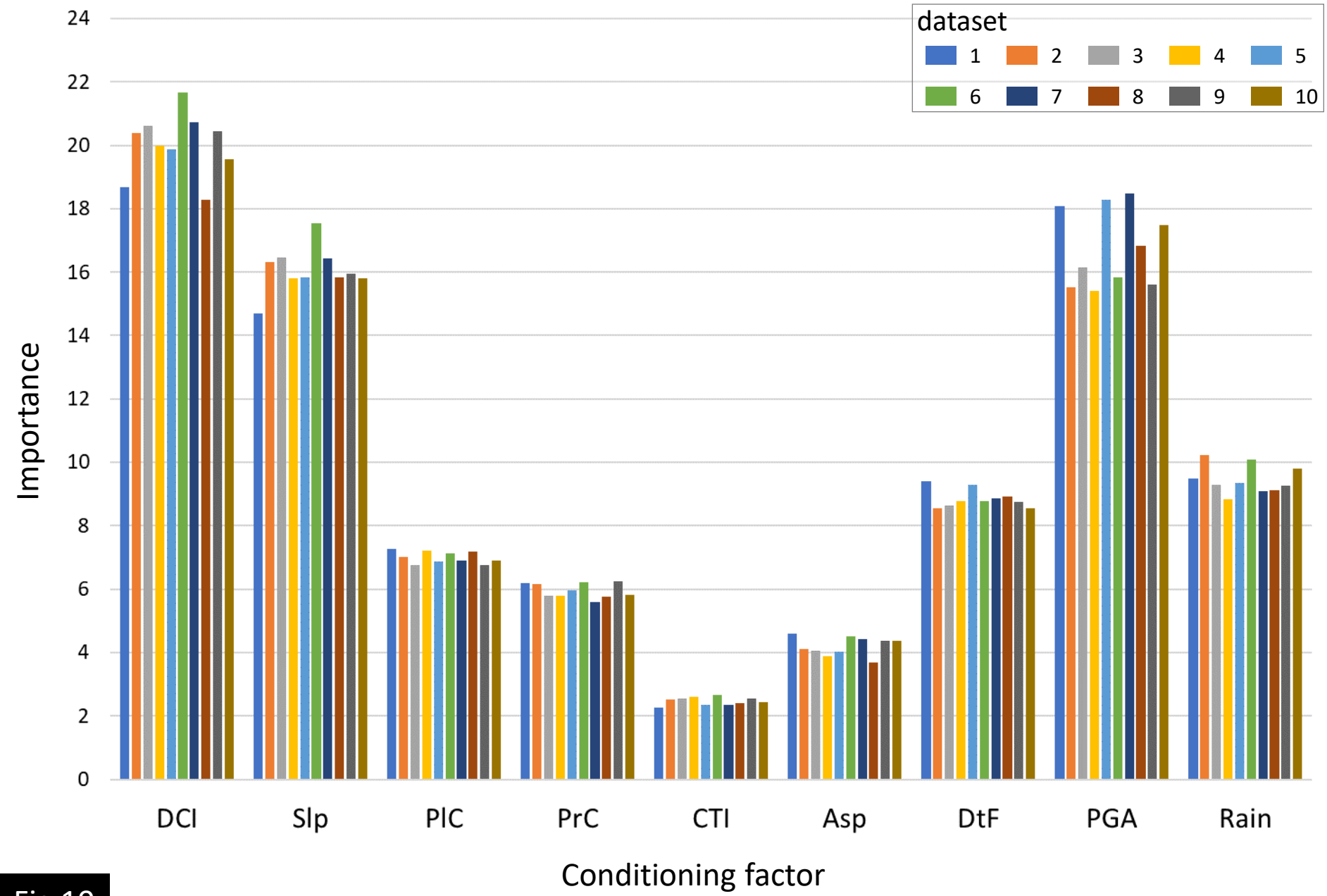
dataset
1
2
3
4
5
6
7
8
9
10
Importance
0
2
4
6
8
10
12
14
16
18
20
22
24
DCl
Slp
PlC
PrC
CTI
Asp
DtF
PGA
Rain
Conditioning factor

Fig 10

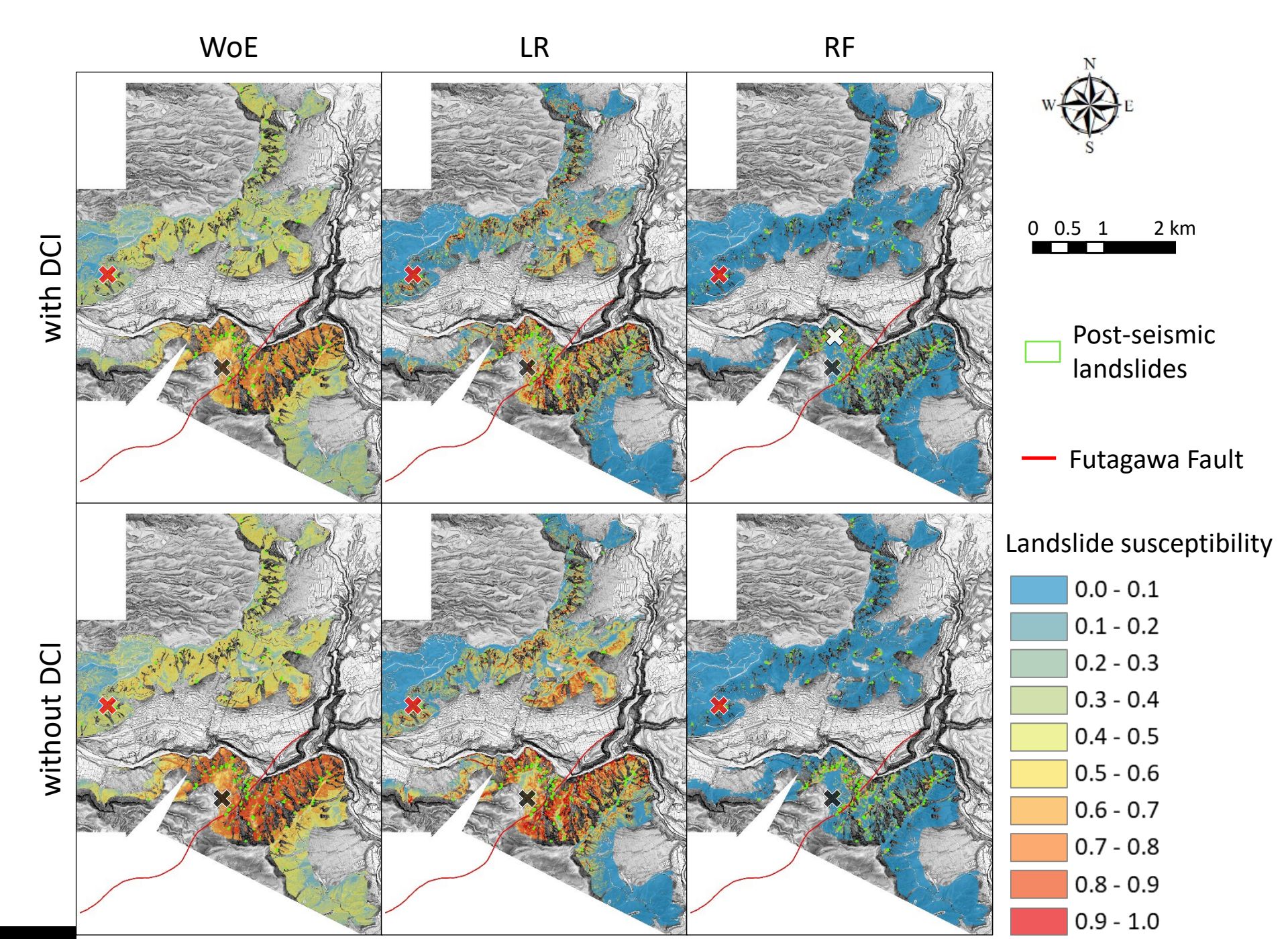
WoE
LR
RF
with DCI
without DCI
N
W
E
S
0 0.5 1 2 km
Post-seismic landslides
Futagawa Fault
Landslide susceptibility
0.0 - 0.1
0.1 - 0.2
0.2 - 0.3
0.3 - 0.4
0.4 - 0.5
0.5 - 0.6
0.6 - 0.7
0.7 - 0.8
0.8 - 0.9
0.9 - 1.0

Fig 11

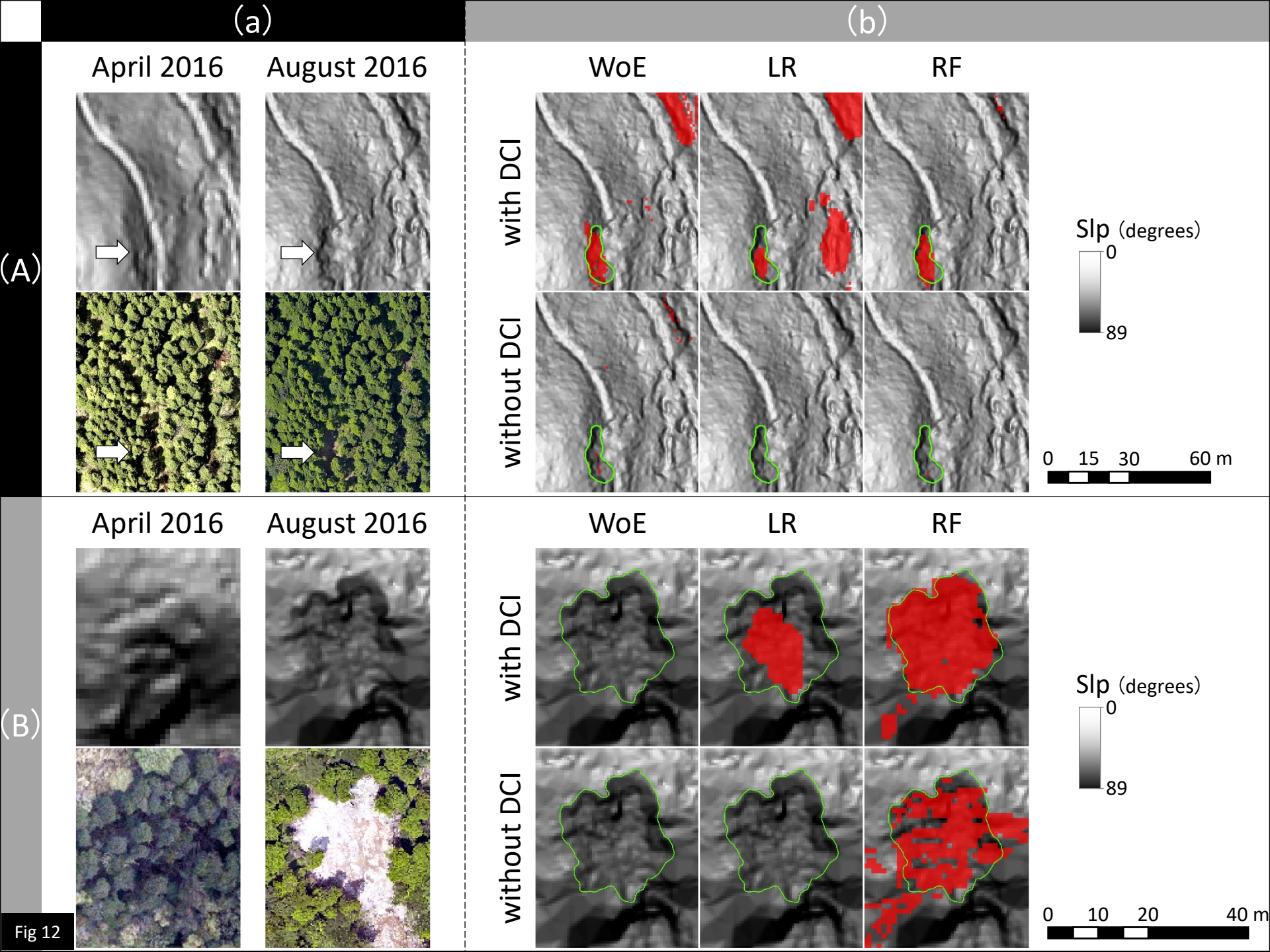
(a)
(b)
(A)
(B)
April 2016
August 2016
WoE
LR
RF
with DCI
without DCI
Slp (degrees)
0
89
0 15 30 60 m
0 10 20 40 m

Fig 12

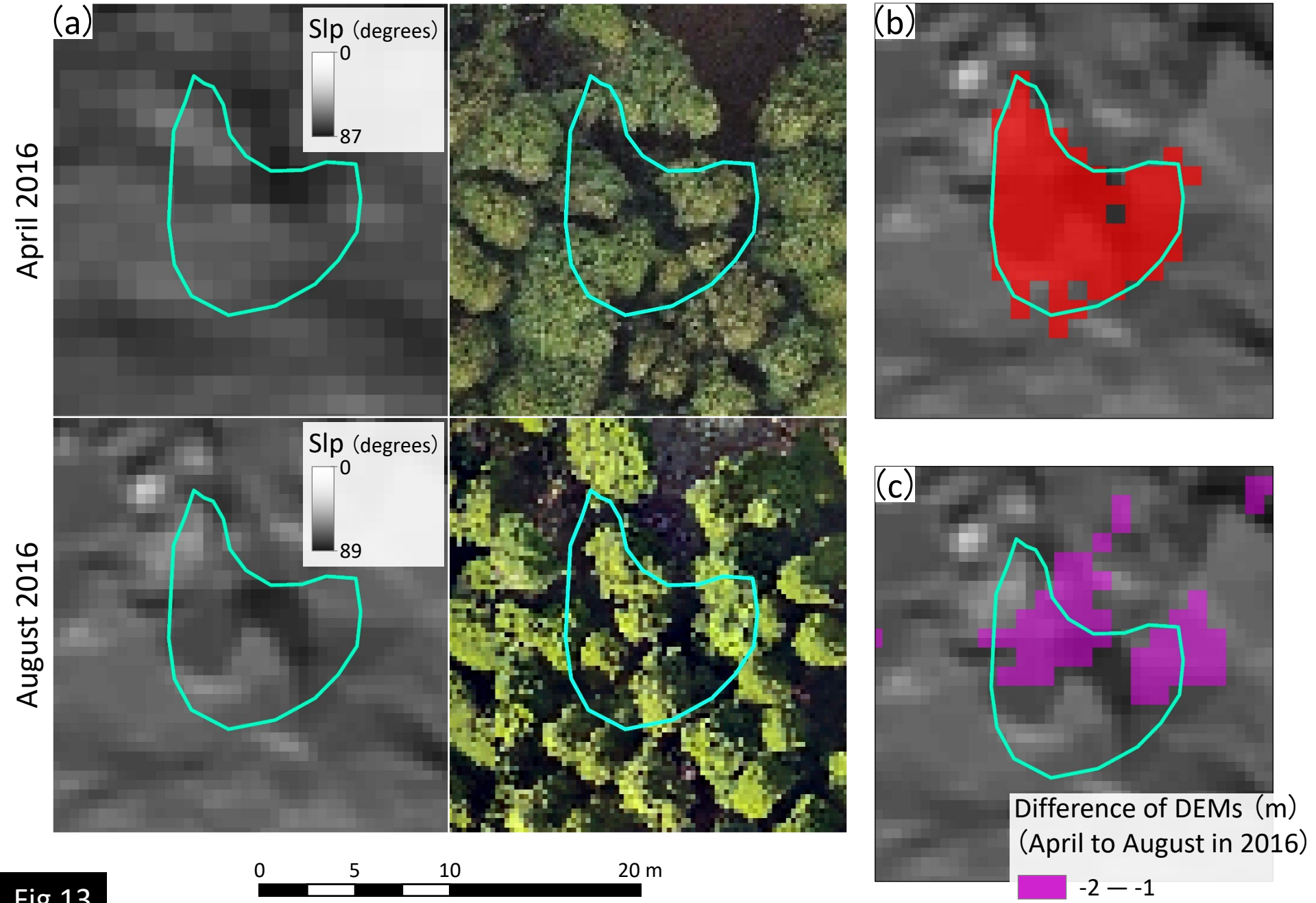
(a)
Slp (degrees)
0
87
Slp (degrees)
0
89
April 2016
August 2016
(b)
(c)
Difference of DEMs（m）
（April to August in 2016）
-2 — -1
0
5
10
20 m

Fig 13